

# A numerical study of the effects of ambient wind direction on flow and dispersion in urban street canyons using the RNG $k$ – $\varepsilon$ turbulence model

Jae-Jin Kim<sup>a</sup>, Jong-Jin Baik<sup>b,\*</sup>

<sup>a</sup>Climate Environment System Research Center, Seoul National University, Seoul 151-742, South Korea

<sup>b</sup>School of Earth and Environmental Sciences, Seoul National University, Seoul 151-742, South Korea

Received 16 October 2003; received in revised form 28 January 2004; accepted 9 February 2004

---

## Abstract

A three-dimensional computational fluid dynamics model with the renormalization group  $k$ – $\varepsilon$  turbulence scheme is developed. The model developed is used to investigate the effects of ambient wind direction on flow and dispersion around a group of buildings. According to the ambient wind direction, three flow patterns are identified in a view of the characteristics of the mean flow circulation generated in street canyons. In the first flow pattern, a portal vortex generated behind the east wall of the upwind building is symmetric about the center of the street canyon. In the second flow pattern, a portal vortex is also generated behind the east wall of the upwind building, but its horizontal axis is not perpendicular to the ambient wind direction. In the third flow pattern, the footprints of a portal vortex are located behind both the east and north walls of the upwind building. When the incident wind angle is  $45^\circ$ , flow is diagonally symmetric behind the upwind building. As the incident wind angle increases, pollutant escape from the street canyons decreases. Except for the case where the ambient wind direction is perpendicular to the buildings, pollutants are trapped in the portal vortex, thus exhibiting high concentration there.

© 2004 Elsevier Ltd. All rights reserved.

**Keywords:** Computational fluid dynamics; RNG  $k$ – $\varepsilon$  turbulence model; Urban flow and dispersion; Urban street canyon; Ambient wind direction

---

## 1. Introduction

People working and living in urban areas are exposed to pollutants emitted from motor vehicles, poisonous gases from unexpected accidents, and chemical and biological toxics from possible attacks by terrorists. The dispersion of those hazardous materials is largely determined by meteorological elements such as ambient wind speed and direction and atmospheric stability and by building configurations such as street and building aspect ratios. During the past two decades, field experiment (e.g., DePaul and Sheih, 1986; Nakamura

and Oke, 1988; Rotach, 1995), physical modeling (wind tunnel or water tank) (e.g., Meroney et al., 1996; Baik et al., 2000; Brown et al., 2000; Uehara et al., 2000), and numerical modeling (e.g., Lee and Park, 1994; Sini et al., 1996; Baik and Kim, 1999; Kim and Baik, 1999, 2001) studies have contributed to our understanding of the effects of meteorological elements and building configurations on flow and dispersion in urban areas (Vardoulakis et al., 2003).

Numerical models are very useful tools not only to do risk assessments of hazardous materials emitted to the atmosphere in urban areas but also to give us desirable guidelines for optimizing ventilation, ensuring sunshine, and reducing heat island effects in urban areas. Various types of numerical models have been employed to simulate urban flow and dispersion.

---

\*Corresponding author. Tel.: +82-2-880-6990; fax: +82-2-883-4972.

Email-address: jjbaik@snu.ac.kr (J.-J. Baik).

Although large-eddy simulation (LES) models attract much interest, their use is restricted because of rather expensive computing times. For this reason, Reynolds-averaged Navier–Stokes equations (RANS) models are widely used in urban flow and dispersion research.

The standard  $k$ – $\varepsilon$  turbulence model that has been commonly used has some deficiencies when it is applied to the simulation of flow impingement and separation (Castro and Apsley, 1997). An improved model over the standard  $k$ – $\varepsilon$  turbulence model is the renormalization group (RNG)  $k$ – $\varepsilon$  turbulence model. Yakhot and Orszag (1986) applied the RNG method to the Navier–Stokes equations and the equations of passive scalar to evaluate turbulence statistics. Smith and Reynolds (1992) identified problems in the Yakhot and Orszag (1986)'s derivation of the equation of turbulent kinetic energy (TKE) dissipation rate. Yakhot and Smith (1992) re-evaluated the constant related to the production of TKE dissipation rate and added an additional production term in the TKE dissipation rate equation. Yakhot et al. (1992) solved the closure problem caused by the additional production term. The main idea of the RNG method lies in the systematic removal of small scales of turbulence by representing their effects in terms of larger-scale motions and a modified viscosity (Yakhot et al., 1992).

The objectives of this study are to develop a three-dimensional computational fluid dynamics (CFD) model with the RNG  $k$ – $\varepsilon$  turbulence scheme and to investigate the effects of ambient wind direction on flow and dispersion in urban areas through numerical simulations using the CFD model developed.

## 2. Model description

The numerical model used in this study is the same as that of Baik et al. (2003) except that the RNG  $k$ – $\varepsilon$  turbulence scheme and wall boundary conditions are implemented. We consider a three-dimensional, nonhydrostatic, nonrotating, incompressible airflow system. The momentum equation, the mass continuity equation, and the transport equation for passive scalar can be written as

$$\frac{\partial U_i}{\partial t} + U_j \frac{\partial U_i}{\partial x_j} = -\frac{1}{\rho_0} \frac{\partial P^*}{\partial x_i} + \nu \frac{\partial^2 U_i}{\partial x_j \partial x_j} - \frac{\partial}{\partial x_j} (\overline{u_i u_j}), \quad (1)$$

$$\frac{\partial U_j}{\partial x_j} = 0, \quad (2)$$

$$\frac{\partial C}{\partial t} + U_j \frac{\partial C}{\partial x_j} = D \frac{\partial^2 C}{\partial x_j \partial x_j} - \frac{\partial}{\partial x_j} (\overline{c u_j}) + S_c. \quad (3)$$

Here,  $U_i$  is the  $i$ th mean velocity component,  $P^*$  is the deviation of pressure from its reference value,  $C$  is

the mean concentration of any passive scalar (say, any pollutant),  $u_i$  and  $c$  are the fluctuations from their respective means  $U_i$  and  $C$ , respectively, and  $\rho_0$  is the air density.  $\nu$  is the kinematic viscosity of air,  $D$  is the molecular diffusivity of pollutant, and  $S_c$  denotes the source term of pollutant.

The Reynolds stress and turbulent flux in (1) and (3) are parameterized in terms of grid-resolvable variables as

$$-\overline{u_i u_j} = K_m \left( \frac{\partial U_i}{\partial x_j} + \frac{\partial U_j}{\partial x_i} \right) - \frac{2}{3} \delta_{ij} k, \quad (4)$$

$$-\overline{c u_j} = K_c \frac{\partial C}{\partial x_j}, \quad (5)$$

where  $K_m$  and  $K_c$  are the turbulent viscosities of momentum and pollutant concentration, respectively,  $\delta_{ij}$  is the Kronecker delta, and  $k$  is the TKE. In the RNG  $k$ – $\varepsilon$  turbulence scheme,  $K_m$  is given by

$$K_m = \nu \left( 1 + \left( \frac{C_\mu}{\nu} \right)^{1/2} \frac{k}{\varepsilon^{1/2}} \right)^2. \quad (6)$$

Here,  $C_\mu$  is an empirical constant. Notice that  $K_m$  in the RNG  $k$ – $\varepsilon$  turbulence scheme includes molecular kinematic viscosity as well. The Schmidt number is expressed by  $Sc (=K_m/K_c)$  and its value is specified as 0.9 to calculate  $K_c$ .

In the present CFD model, the RNG  $k$ – $\varepsilon$  turbulence scheme presented by Yakhot et al. (1992) is used. This scheme differs from the standard  $k$ – $\varepsilon$  turbulence scheme in that it includes an additional sink term in the turbulence dissipation equation to account for non-equilibrium strain rates and employs different values for the model coefficients (Tutar and Oguz, 2002). The prognostic equations of turbulent kinetic energy and its dissipation rate can be written as

$$\frac{\partial k}{\partial t} + U_j \frac{\partial k}{\partial x_j} = -\overline{u_i u_j} \frac{\partial U_i}{\partial x_j} + \frac{\partial}{\partial x_j} \left( \frac{K_m}{\sigma_k} \frac{\partial k}{\partial x_j} \right) - \varepsilon, \quad (7)$$

$$\begin{aligned} \frac{\partial \varepsilon}{\partial t} + U_j \frac{\partial \varepsilon}{\partial x_j} = & -C_{\varepsilon 1} \frac{\varepsilon}{k} \overline{u_i u_j} \frac{\partial U_i}{\partial x_j} + \frac{\partial}{\partial x_j} \left( \frac{K_m}{\sigma_\varepsilon} \frac{\partial \varepsilon}{\partial x_j} \right) \\ & - C_{\varepsilon 2} \frac{\varepsilon^2}{k} - R, \end{aligned} \quad (8)$$

where  $\sigma_k$ ,  $\sigma_\varepsilon$ ,  $C_{\varepsilon 1}$ , and  $C_{\varepsilon 2}$  are empirical constants. The last term on the right-hand side of Eq. (8) is an extra strain rate term given by

$$R = \frac{C_\mu \eta^3 (1 - \eta/\eta_0) \varepsilon^2}{(1 + \beta_0 \eta^3) k}, \quad (9)$$

$$\eta = \frac{k}{\varepsilon} \left[ \left( \frac{\partial U_i}{\partial x_j} + \frac{\partial U_j}{\partial x_i} \right) \frac{\partial U_i}{\partial x_j} \right]^{1/2}. \quad (10)$$

The constants in the RNG  $k$ - $\varepsilon$  turbulence scheme are specified as (Yakhot et al., 1992):

$$(C_\mu, \sigma_k, \sigma_\varepsilon, C_{\varepsilon 1}, C_{\varepsilon 2}, \beta_0, \eta_0) \\ = (0.0845, 0.7179, 0.7179, 1.42, 1.68, 0.012, 4.377). \quad (11)$$

In modeling urban flow and dispersion, smaller grid sizes are desirable near buildings to better resolve flow and dispersion fields there, but away from buildings larger grid sizes are allowable. To make the CFD model efficient for a given computing resource, a non-uniform grid system is implemented in the model, following Versteeg and Malalasekera (1995). The governing equation set is numerically solved on a staggered grid system using a finite volume method with the semi-implicit method for pressure-linked equation (SIMPLE) algorithm (Patankar, 1980). For further details of the numerical procedure, see Baik et al. (2003).

### 3. Experimental setup

To study the effects of ambient wind direction on flow and pollutant dispersion in urban areas, a group of buildings are considered and a non-uniform grid system with 101 cells in the  $x$ - and  $y$ -directions and 41 cells in

the  $z$ -direction is used (Fig. 1). The dimension of the smallest cell is  $0.3 \text{ m} \times 0.3 \text{ m} \times 0.3 \text{ m}$  in the  $x$ -,  $y$ -, and  $z$ -directions, which is situated at the edges of the buildings. The expansion ratio in the present non-uniform grid system is 1.1. The largest cell dimension is  $1.8 \text{ m} \times 1.8 \text{ m} \times 1.8 \text{ m}$ . Castro and Apsley (1997) used an expansion ratio of 1.07 and Zhang et al. (1996) used expansion ratios not exceeding 1.3. The computational domain size is  $63.1 \text{ m} \times 63.1 \text{ m} \times 28.5 \text{ m}$  in the  $x$ -,  $y$ -, and  $z$ -directions, respectively. Four buildings located around the center of the domain are cubic. The street width ( $W$ ) between the buildings is the same as the building length ( $L$ ) and the building height ( $H$ ). So, the street aspect ratios,  $H/W$  and  $L/W$ , are all equal to 1. For convenience, the street canyons between the buildings I and II, II and III, III and IV, and IV and I (Fig. 1) are called west, south, east, and north street canyons, respectively. The time step used is 0.05 s. For better resolving small-scale fluctuations in time, a relatively small time step is used. The numerical model is integrated up to  $t = 20 \text{ min}$ . An investigation of time dependency indicated that a quasi-steady state in the flow field is established after  $t = 5\text{--}7 \text{ min}$ . Passive pollutants are continuously released from the centers of the first cells above the ground surface ( $z = 0.15 \text{ m}$ ) between the four buildings starting from  $t = 10 \text{ min}$ . It is assumed that pollutants released are homogeneously distributed in the source cells and that pollutants are released with an emission rate of  $10 \text{ ppbs}^{-1}$  at each source cell. All simulation results presented below are at  $t = 20 \text{ min}$  except for Fig. 2, which is at  $t = 10 \text{ min}$ .

The vertical profiles of ambient wind and TKE and its dissipation rate (inflow boundary conditions) are specified as (Castro and Apsley, 1997):

$$U_{\text{in}}(z) = \frac{U_*}{\kappa} \ln\left(\frac{z}{z_0}\right) \cos \theta, \quad (12)$$

$$V_{\text{in}}(z) = \frac{U_*}{\kappa} \ln\left(\frac{z}{z_0}\right) \sin \theta, \quad (13)$$

$$W_{\text{in}}(z) = 0, \quad (14)$$

$$k_{\text{in}}(z) = \frac{1}{C_\mu^{1/2}} U_*^2 \left(1 - \frac{z}{\delta}\right)^2, \quad (15)$$

$$\varepsilon_{\text{in}}(z) = \frac{C_\mu^{3/4} k_{\text{in}}^{3/2}}{\kappa z}, \quad (16)$$

where  $U_*$ ,  $\theta$ ,  $z_0$ ,  $\delta$ , and  $\kappa$  are the friction velocity, wind direction (measured counterclockwise from the positive  $x$ -axis), roughness length ( $=0.05 \text{ m}$ ), boundary layer depth ( $=100 \text{ m}$ ), and von Karman constant ( $=0.4$ ), respectively. At the outflow and upper boundaries, zero-gradient condition is applied. At the solid surface, wall boundary conditions are applied, following Versteeg and Malalasekera (1995) (Table 1).

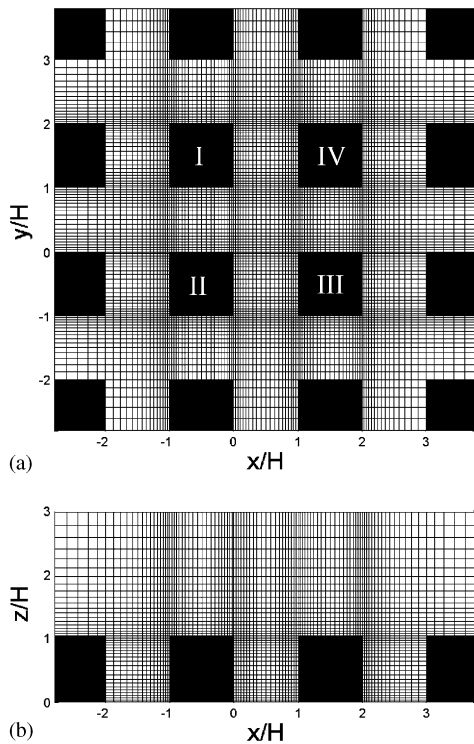


Fig. 1. The (a) top view and (b) side view of the computational domain and grid system.

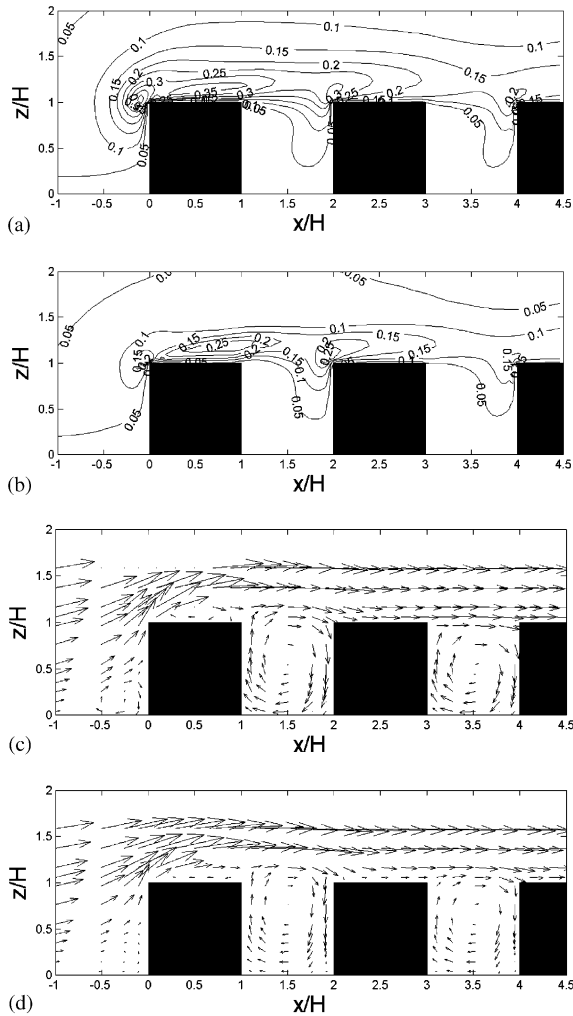


Fig. 2. The normalized TKE fields ( $k/(0.5U_r^2)$ ) simulated by the (a) standard and (b) RNG  $k$ - $\epsilon$  turbulence schemes and wind vector fields normalized by the upstream horizontal velocity ( $U_r$ ) at the reference height ( $H$ ) in the cases of the (c) wind tunnel (Brown et al., 2000) and (d) RNG simulation.

#### 4. Model validation

The three-dimensional CFD model with the RNG  $k$ - $\epsilon$  turbulence scheme is compared with that using the standard  $k$ - $\epsilon$  turbulence scheme and validated against the wind tunnel data of Brown et al. (2000). The building configuration follows their 2-D array of buildings. The ambient wind direction is perpendicular to the building ( $\theta = 0^\circ$ ). The simulated data are interpolated at the same grid points in the wind tunnel experiment. The results are presented in Fig. 2. The TKE field simulated with the RNG  $k$ - $\epsilon$  turbulence scheme reproduces flow separation and reverse flow above the first building (Figs. 2c and d) by reducing an

Table 1

Near wall relations (from Versteeg and Malalasekera, 1995)

- Momentum equation tangential to wall  
Wall shear stress  $\tau_w = \rho C_\mu^{1/4} k_p^{1/2} u_p / u^+$   
Wall force  $F_s = -\tau_w A_{\text{cell}}$
- Momentum equation normal to wall  
Normal velocity = 0
- TKE equation  
Net  $k$ -source per unit volume  $S_k = (\tau_w u_p - \rho C_\mu^{3/4} k_p^{3/2} u^+) \Delta V / \Delta y_p$
- Dissipation rate equation  
Set nodal value  $\epsilon_p = C_\mu^{3/4} k_p^{3/2} / (\kappa \Delta y_p)$

Here,  $u^+$ ,  $A_{\text{cell}}$ , and  $\Delta y$  are the non-dimensional velocity, wall area of the control volume ( $\Delta V$ ), and the distance to the solid surface. The subscript  $p$  denotes the nearest wall node.

unphysical anomaly of TKE near the upwind edge of the first building in the simulation using the standard  $k$ - $\epsilon$  turbulence scheme (Figs. 2a and b). Although the horizontal and vertical wind velocities are underestimated to some extent in the second street canyon (Figs. 2c, d, 3a and 3b), the main features of the mean flow (roll-type vortices in front of the first building and in the street canyons and recirculation above the first building roof) are simulated well (Figs. 2c and d). The maximum TKE at each position appears above the roof level of the street canyon in both the experiments, but the numerical model underestimates TKE at most heights (Fig. 3c). However it is expected that more accurate information on TKE at the inflow boundary can give a better simulation result. Based on reasonably good agreement the CFD model developed can be applied to the simulation of flow and dispersion in urban areas.

Tutar and Oguz (2002) showed that even the standard  $k$ - $\epsilon$  turbulence scheme can produce flow separation at the front corner of the building and reverse flow on the roof of the building with fine grid resolution. Similar to their result, we were also able to find those features, but occasionally in time, using the standard  $k$ - $\epsilon$  turbulence scheme.

#### 5. Results and discussion

##### 5.1. Flow characteristics

Ten cases with different ambient wind directions are simulated and analyzed. The ambient wind direction ( $\theta$ ) varies from  $0^\circ$  to  $45^\circ$  with an increment of  $5^\circ$ . Notice that if the ambient wind direction has an angle of  $0^\circ < \theta \leq 45^\circ$ , the west and south edges of the computational domain are inflow boundaries. According to the ambient wind direction, simulated flows can be classified

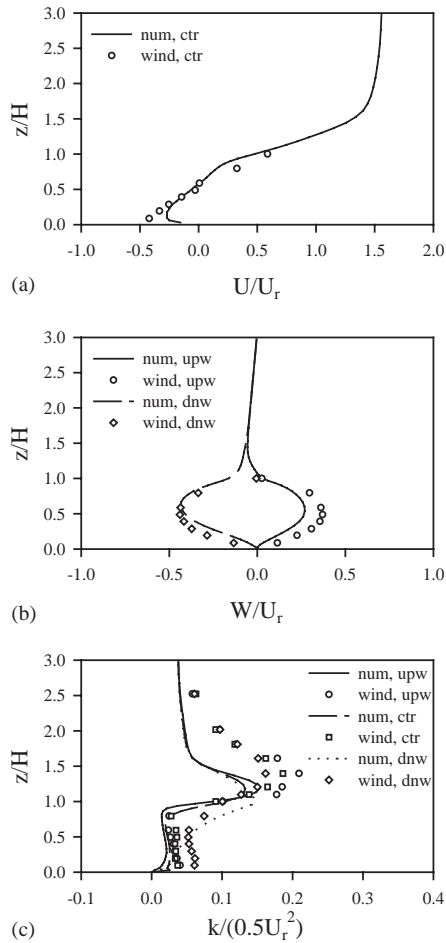


Fig. 3. The vertical profiles of (a) normalized horizontal velocity at  $x = 0.5H$ , (b) normalized vertical velocity at  $x = 0.1H$  and  $0.9H$ , and (c) normalized TKE at  $x = 0.1H$ ,  $0.5H$ , and  $0.9H$ . All data are obtained in the second street canyon. The num, wind, upw, ctr, and dnw denote the numerical result, wind tunnel result, upwind ( $x = 0.1H$ ), center ( $x = 0.5H$ ), and downwind ( $x = 0.9H$ ), respectively.

into three patterns in a view of the characteristics of the mean flow circulation generated behind the upwind building. The schematic of each flow pattern is presented in Fig. 4, which is drawn based on simulated flow analysis.

**Flow pattern I:** The first flow pattern appears when the ambient wind direction is perpendicular to the buildings ( $\theta = 0^\circ$ ). In this case, flow is symmetric about the center of the street canyon (Fig. 4a). Near the upwind building, flow is upward and outward. Near the downwind building, flow is downward and inward in the upper region, but it is downward and outward in the lower region. Near the street bottom, flow is predominantly outward. Behind the upwind building, there exists a portal vortex (Becker et al., 2002) whose ends are

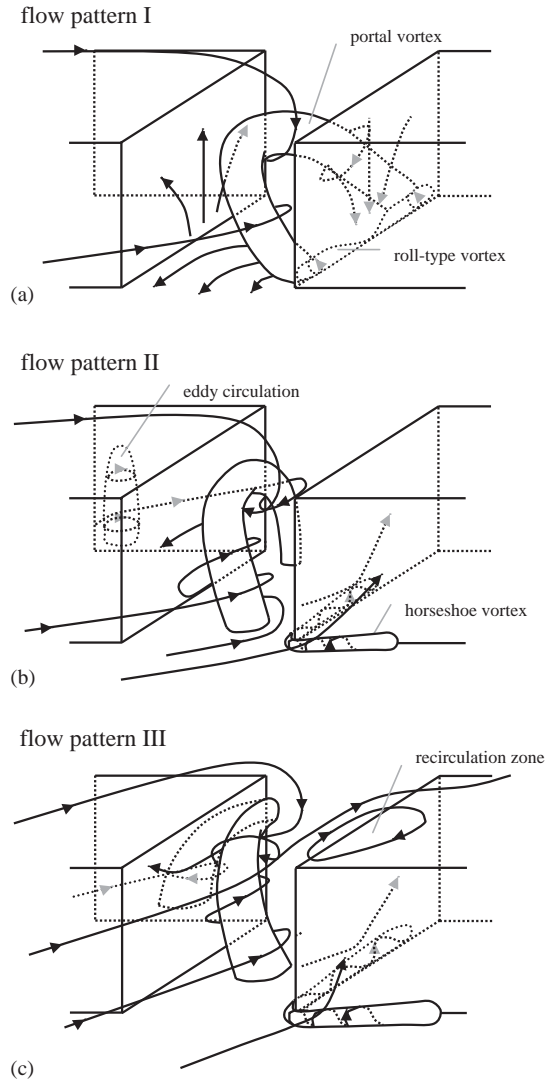


Fig. 4. The schematic of the mean flow circulation according to different ambient wind directions. The dimensions of the portal vortex depicted here are reduced for the clarity of figure.

located near the lower edges of the downwind building. The portal vortex is symmetric about the center of the street canyon and its horizontal axis is perpendicular to the ambient wind direction. Flow coming into the street canyon curls up around the portal vortex. At the center of the street canyon, there is apparently no motion in the  $y$ -direction. The roll-type vortex rotating anticlockwise from the south view appears at the corner between the street bottom and the downwind building and it disappears near the center of the street canyon. All the features mentioned above can be identified in the cross-sectional wind vector plots (Fig. 5). The  $x$ - $y$  plane wind vector field at  $z/H = 0.5$  shows symmetric double-vortex (or called double-eddy) circulations (Fig. 5a).



The  $x$ – $z$  plane wind vector field at  $y/H = -0.75$  exhibits the cross-section of the portal vortex and the small vortex rotating anticlockwise near the corner of the downwind building (Fig. 5b). Inward and downward flow is stronger than upward and outward flow, especially near the street canyon center. By mass conservation, this results in the whole outward motion near the street bottom. Consequently, the footprints of the portal vortex are located near the southwest and northwest edges of the downwind building. The  $y$ – $z$  plane wind vector field at  $x/H = 0.5$  shows two symmetric vortices (Fig. 5c). This is evidence that the top of the portal vortex is slightly tilted towards the upwind region. Notice that outward flow is dominant near the street bottom.

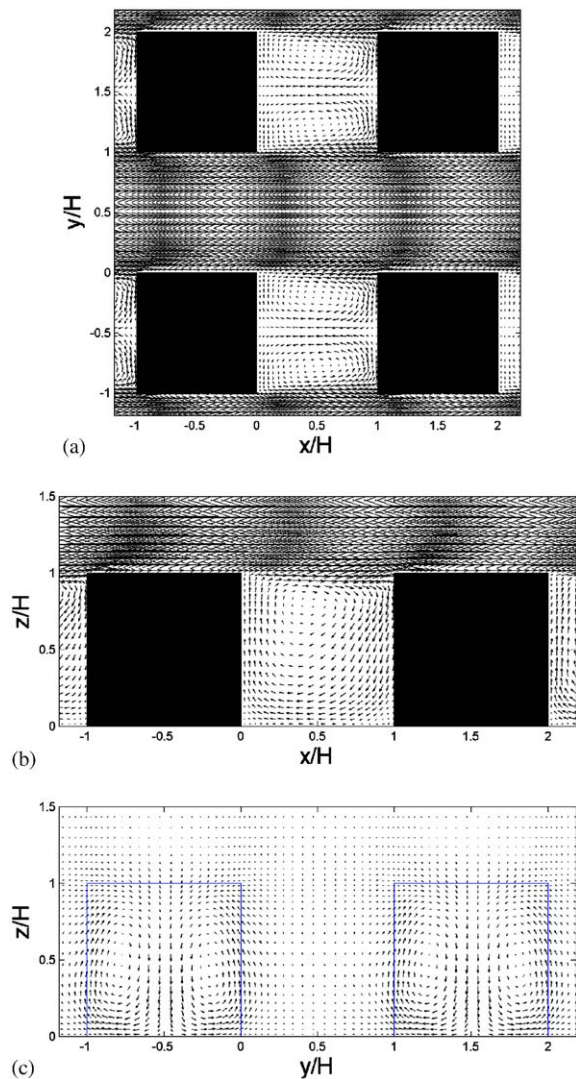


Fig. 5. The wind vector fields at (a)  $z/H = 0.5$ , (b)  $y/H = -0.75$ , and (c)  $x/H = 0.5$  in the case of  $\theta = 0^\circ$ .

*Flow pattern II:* The second flow pattern appears when  $5^\circ \leq \theta \leq 20^\circ$  (Fig. 4b). Similar to flow pattern I, a portal vortex is also generated. However, in flow pattern II, one footprint of the portal vortex is located near the street center and the other near the northeast edge of the upwind building (Fig. 4b). The difference in footprint position is associated with the wind direction near the street bottom. In flow pattern II, northeastward inflow from the canyon south is dominant near the southeast region of the street canyon. This causes the portal vortex to be detached from the downwind building. Near the north wall of the upwind building, an eddy circulation, which is absent in flow pattern I, is generated (Fig. 6a). The eddy circulation rotating clockwise is induced by flow separation. Incoming flow from the canyon south

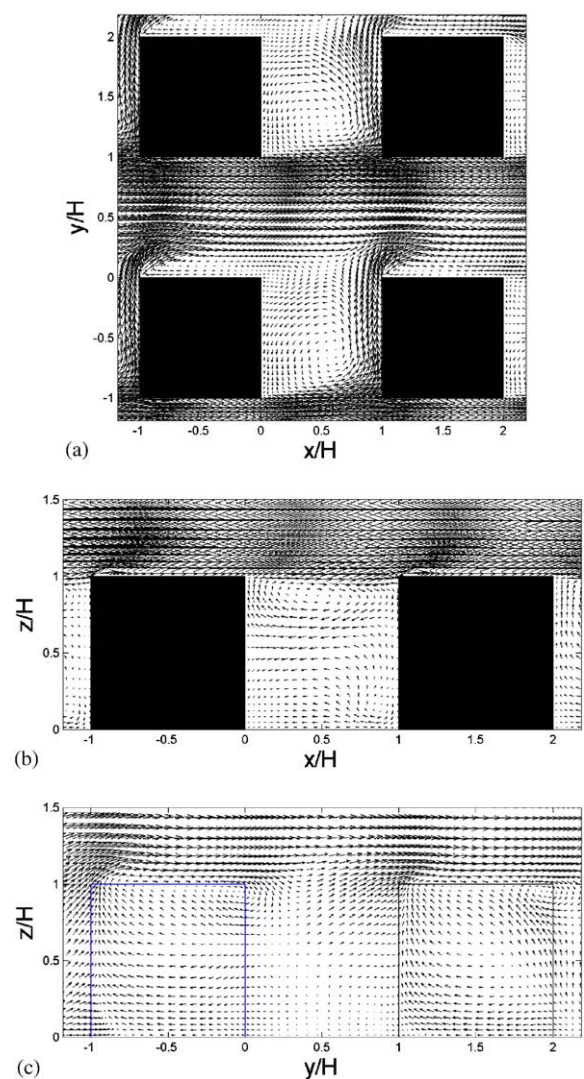


Fig. 6. The wind vector fields at (a)  $z/H = 0.5$ , (b)  $y/H = -0.75$ , and (c)  $x/H = 0.25$  in the case of  $\theta = 15^\circ$ .

impinges on the building, producing stagnation point on the south and west walls of the downwind building and accordingly forming a horseshoe vortex around the building (Fig. 6b). The stagnation point due to flow impingement is also produced at the west and south walls of the upwind building. In flow pattern II, the horizontal axis of the portal vortex is not perpendicular to the ambient wind direction (Fig. 6a). Further investigation of the  $x$ - $z$  plane wind vector field reveals that the angle between the horizontal axis of the portal vortex and ambient wind direction varies with height. The angle is closer to being perpendicular to the ambient wind direction in the upper region than in the lower region.

**Flow pattern III:** This flow pattern occurs when  $25^\circ \leq \theta \leq 45^\circ$ . A portal vortex is also generated and its footprints are located behind the north and east walls of the upwind building (Fig. 4c). As the incident wind angle increases, the horizontal size of the portal vortex behind the east wall decreases, but that behind the north wall increases. As in flow pattern II, a horseshoe vortex is also generated along the south and west walls of the building. When the incident wind angle is  $45^\circ$ , flow is diagonally symmetric behind the upwind building (Fig. 7a). Above the building roof, recirculation zones are generated due to flow separation as flow impinges on the buildings (Fig. 7b). The  $y$ - $z$  plane wind vector field at  $x/H = 0.25$  shows a clockwise rotating vortex, which is evidence that the top of the portal vortex is slightly tilted towards the upwind region (Fig. 7c).

The grid dependency was tested using two uniform grid systems with  $67 \times 67 \times 31$  and  $100 \times 100 \times 41$  cells in the  $x$ -,  $y$ -, and  $z$ -directions, respectively, and simulation results were compared with those using the non-uniform grid system with 101 cells in the  $x$ - and  $y$ -directions and 41 cells in the  $z$ -direction, when the ambient wind direction ( $\theta$ ) is  $0^\circ$  and  $45^\circ$ . Results showed that the main flows such as portal vortex are simulated in each case and their sizes are similar to one another, but the cases using the uniform grid systems fail to reproduce flow separation and reverse flow above the building roof in the case of  $\theta = 45^\circ$  because of relatively coarse resolution near the building roof. For this reason, the non-uniform grid system was adopted in this study.

## 5.2. Dispersion characteristics

To examine the effects of ambient wind direction on scalar dispersion, pollutant sources are located close to the street bottom ( $z = 0.15$  m,  $z/H = 0.02$ ) in the east, west, south, and north street canyons and crossroad area between them. In this study, pollutant advection from the upwind region is not considered. Fig. 8 shows pollutant concentration fields at  $z = 1.6$  m (pedestrian level,  $z/H = 0.17$ ) in the cases of  $\theta = 0^\circ$ ,  $15^\circ$ , and  $45^\circ$ .

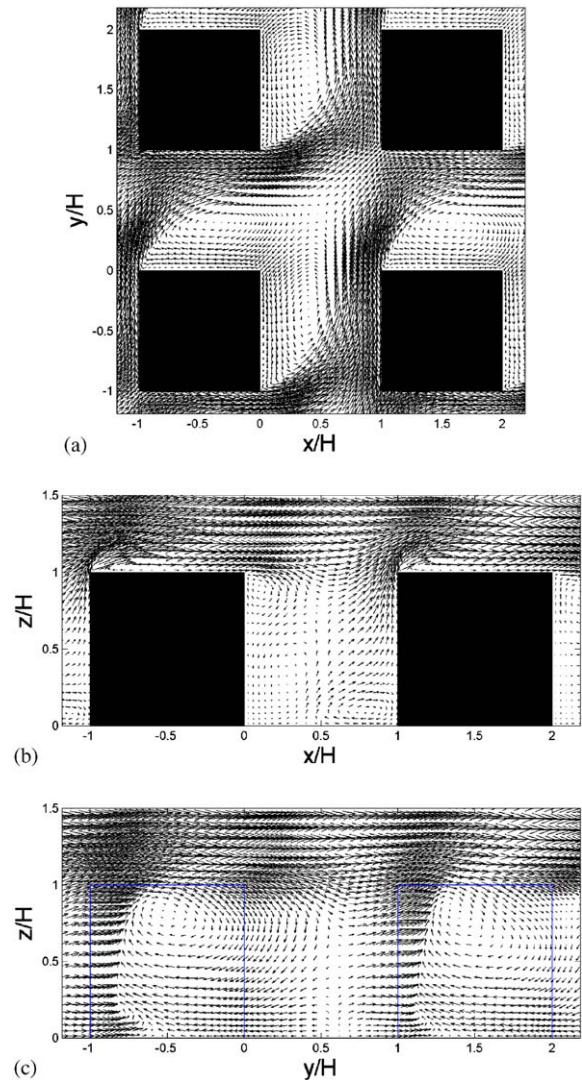


Fig. 7. The same as in Fig. 6 except for the case of  $\theta = 45^\circ$ .

Pollutant concentration (in units of ppb) is presented on a logarithmic scale in base 10.

In the case of  $\theta = 0^\circ$  (Fig. 8a), very low concentration in the south (north) street canyon appears as going to the street-canyon center region from the downwind building because of inward and downward inflow having relatively low concentration. It is unexpected that in the south (north) street canyon pollutants are not trapped in the two vortices and the maximum concentration does not appear near the centers of the vortices. Concentration is relatively high near the upwind building and the south and north verges of the street canyon. Notice that the lowest concentration in the street canyon appears near the downwind building. Concentration in the west street canyon is very low. This means that most pollutants emitted are transported downwind before

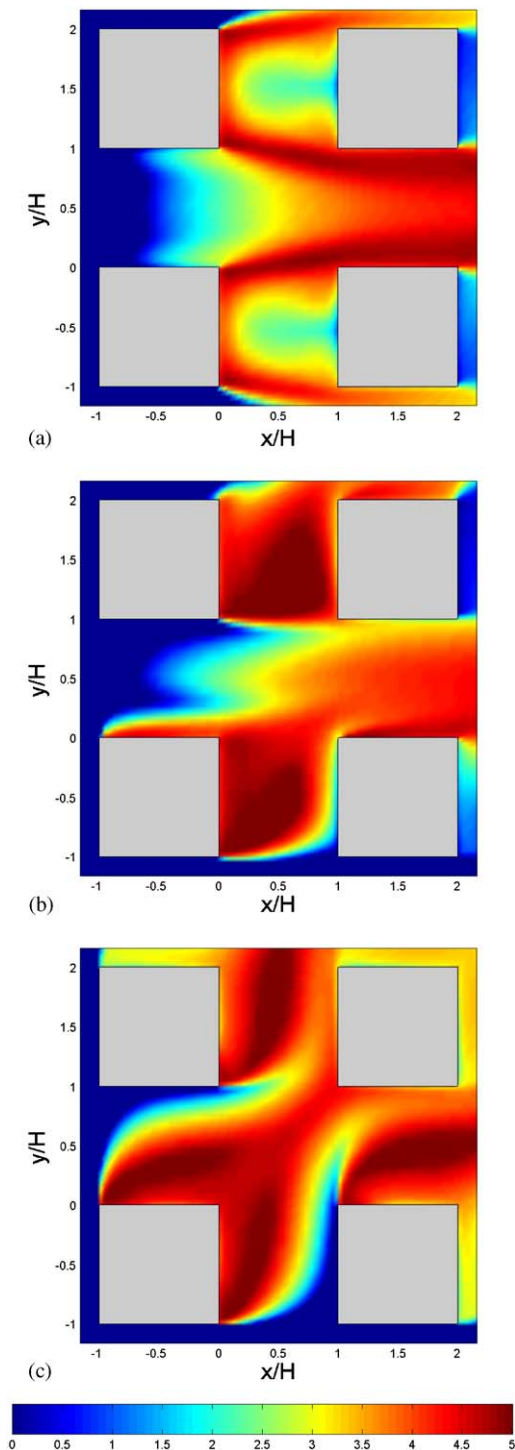


Fig. 8. Concentration fields (log scale in base 10) at  $z/H = 0.17$  in the cases of (a)  $\theta = 0^\circ$ , (b)  $\theta = 15^\circ$ , and (c)  $\theta = 45^\circ$ .

they are transported upward. There are high concentration bands beginning from the southeast and northeast edges of the upwind building. The bands extend down-

wind. Near the upwind building, pollutants transported to both sides of the street canyon by outward flow are transported upward by vertical motion (Fig. 5c) and then escape from the street canyon. This explains why pollutants are not trapped in the vortices.

Unlike in the case of  $\theta = 0^\circ$ , in the case of  $\theta = 15^\circ$  (Fig. 8b), the maximum concentration appears near the center of the larger vortex in the south (north) street canyon and concentration is relatively high around the larger vortex center. Low concentration appears in the west street canyon and the southeast region of the south street canyon. Concentration near the south wall of the building I is lower than in the case of  $\theta = 0^\circ$ . Concentration in the downwind region is very low in the south street canyon but relatively high in the north street canyon. The fact that there is no emission source outside of the central four buildings gives an explanation for the difference. In the south street canyon, relatively clean air continuously comes into the street canyon from outside and it dilutes polluted air. On the other hand, in the north street canyon, the incoming air is already polluted by passing through the emission sources, thus increasing concentration. The local maximum also appears near the northeast edge of the upwind building where the portal vortex exists. Pollutants are trapped along the north wall of the upwind building where flow is separated and eddy circulation is generated (Fig. 6a).

In the case of  $\theta = 45^\circ$  (Fig. 8c), concentration field is diagonally symmetric. Four high concentration regions appear around the centers of the vortices as pollutants emitted are trapped within the vortices. Concentration is very low in the southeast region of the south street canyon and in the northwest region of the west street canyon where relatively clean air arrives.

In Section 5.1, it is found that flow in street canyons largely depends on ambient wind direction. Therefore, it is not straightforward to intercompare results obtained through different numerical simulations using a point-based method. Instead, results are intercompared by calculating the residue concentration ratio, which is defined as the ratio of the total amount of pollutants remaining in the four street canyons and the crossroad to the total amount of pollutants emitted during the integration (Kim and Baik, 1999). The calculated results are plotted in Fig. 9. As a whole, the residue concentration ratio increases as the ambient wind direction increases despite very little differences among the cases except for the case of  $\theta = 0^\circ$  (Fig. 9). When  $\theta = 0^\circ$ , the residue concentration ratio is relatively much smaller than that in other cases. This is because in the case of  $\theta = 0^\circ$  outward flow is dominant near the street bottom, which makes it easier for pollutant transport to the outside of the street canyon. We also investigate how much each street canyon contributes to the residue concentration ratio (Fig. 9). In the west street canyon, the residue concentration ratio increases rather rapidly



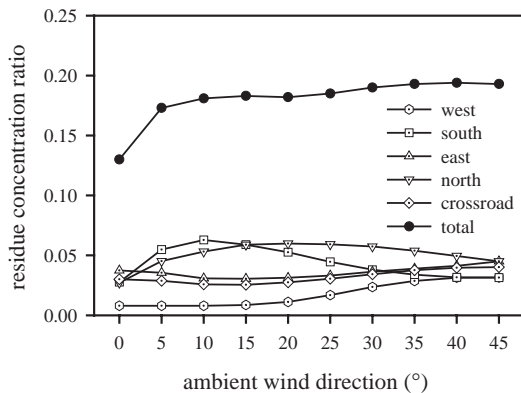


Fig. 9. The residue concentration ratio as a function of ambient wind direction.

from  $\theta = 20^\circ$ . This results from pollutant trapping due to flow separation and eddy circulation there. When  $5^\circ \leq \theta \leq 20^\circ$ , the residue concentration ratio in the south and north street canyons is large due to pollutant trapping by the portal vortex. However, when  $\theta \geq 25^\circ$ , the residue concentration ratio in the south street canyon decreases rapidly due to the incoming clean air, but that in the north street canyon decreases slowly as pollutants emitted elsewhere are transported. Variations in the residue concentration ratio are relatively small in the east street canyon and the crossroad. In flow pattern II, pollutant amount trapped in the south and north street canyons is much larger than that in the east street canyon and the crossroad.

## 6. Summary and conclusion

A three-dimensional CFD model with the RNG  $k-\epsilon$  turbulence scheme was developed and was used to investigate the effects of ambient wind direction on flow and dispersion around a group of buildings.

According to the ambient wind direction, three flow patterns could be classified in a view of the characteristics of the mean flow circulation generated behind the upwind building. In the first flow pattern, a portal vortex generated behind the east wall of the upwind building is symmetric about the center of the street canyon. Near the street bottom, outward flow is dominant, which makes the footprints of the portal vortex be located near the lower edges of the downwind building. Also, a roll-type standing vortex is generated at the corner between the street bottom and the downwind building. In the second flow pattern, a portal vortex is also generated behind the east wall of the upwind building. Its footprints are located near the center of the street canyon and the northeast edge of the upwind building. The horizontal size of the south-side portal vortex is

larger than that of the north-side one. The portal vortex is slightly tilted anticlockwise in the horizontal. An eddy circulation is generated behind the north wall of the upwind building where flow separates. In the third flow pattern, a portal vortex is generated and its footprints are located behind the east and north walls of the upwind building. When the incident wind angle is  $45^\circ$ , flow is diagonally symmetric behind the upwind building. A horseshoe vortex is generated in front of the building. As the incident wind angle increases, pollutant escape from the street canyons decreases. Except for the case of  $\theta = 0^\circ$ , pollutants are trapped in the portal vortex and high concentration appears there. When  $\theta = 0^\circ$ , pollutants are transported to both side verges of the street canyon by outward flow dominant near the street bottom. Then, pollutants escape from the street canyon.

This study demonstrated that changes in ambient wind direction can make large differences in the mean flow circulation and accordingly the spatial distribution of passive pollutants. It is concluded that the ambient wind direction can greatly affect flow and dispersion around a group of buildings.

## Acknowledgements

The authors thank two anonymous reviewers for providing valuable comments on this study. This research was supported by the Climate Environment System Research Center sponsored by the SRC Program of the Korea Science and Engineering Foundation and also by the Brain Korea 21 Project.

## References

- Baik, J.-J., Kim, J.-J., 1999. A numerical study of flow and pollutant dispersion characteristics in urban street canyons. *Journal of Applied Meteorology* 38, 1576–1589.
- Baik, J.-J., Park, R.-S., Chun, H.-Y., Kim, J.-J., 2000. A laboratory model of urban street-canyon flows. *Journal of Applied Meteorology* 39, 1592–1600.
- Baik, J.-J., Kim, J.-J., Fernando, H.J.S., 2003. A CFD model for simulating urban flow and dispersion. *Journal of Applied Meteorology* 42, 1636–1648.
- Becker, S., Lienhart, H., Durst, F., 2002. Flow around three-dimensional obstacles in boundary layers. *Journal of Wind Engineering and Industrial Aerodynamics* 90, 265–279.
- Brown, M.J., Lawson Jr. R.E., DeCroix, D.S., Lee, R.L., 2000. Mean flow and turbulence measurements around a 2-D array of buildings in a wind tunnel. 11th Joint Conference on the Applications of Air Pollution Meteorology with the A&WMA, Long Beach, CA, USA, pp. 35–40.
- Castro, I.P., Apsley, D.D., 1997. Flow and dispersion over topography: a comparison between numerical and laboratory data for two-dimensional flows. *Atmospheric Environment* 31, 839–850.

- DePaul, F.T., Sheih, C.M., 1986. Measurements of wind velocities in a street canyon. *Atmospheric Environment* 20, 455–459.
- Kim, J.-J., Baik, J.-J., 1999. A numerical study of thermal effects on flow and pollutant dispersion in urban street canyons. *Journal of Applied Meteorology* 38, 1249–1261.
- Kim, J.-J., Baik, J.-J., 2001. Urban street-canyon flows with bottom heating. *Atmospheric Environment* 35, 3395–3404.
- Lee, I.Y., Park, H.M., 1994. Parameterization of the pollutant transport and dispersion in urban street canyons. *Atmospheric Environment* 28, 2343–2349.
- Meroney, R.N., Pavageau, M., Rafailidis, S., Schatzmann, M., 1996. Study of line source characteristics for 2-D physical modelling of pollutant dispersion in street canyon. *Journal of Wind Engineering and Industrial Aerodynamics* 62, 37–56.
- Nakamura, Y., Oke, T.R., 1988. Wind, temperature, and stability conditions in an east–west oriented urban canyon. *Atmospheric Environment* 22, 2691–2700.
- Patankar, S.V., 1980. *Numerical Heat Transfer and Fluid Flow*. McGraw-Hill, New York pp. 126–131.
- Rotach, M.W., 1995. Profiles of turbulence statistics in and above an urban street canyon. *Atmospheric Environment* 29, 1473–1486.
- Sini, J.-F., Anquetin, S., Mestayer, P.G., 1996. Pollutant dispersion and thermal effects in urban street canyons. *Atmospheric Environment* 30, 2659–2677.
- Smith, L.M., Reynolds, W.C., 1992. On the Yakhot–Orszag renormalization group method for deriving turbulence statistics and models. *Physics of Fluids A* 4, 364–390.
- Tutar, M., Oguz, G., 2002. Large eddy simulation of wind flow around parallel buildings with varying configurations. *Fluid Dynamics Research* 31, 289–315.
- Uehara, K., Murakami, S., Oikawa, S., Wakamatsu, S., 2000. Wind tunnel experiments on how thermal stratification affects flow in and above urban street canyons. *Atmospheric Environment* 34, 1553–1562.
- Vardoulakis, S., Fisher, B.E.A., Pericleous, K., Gonzalez-Flesca, N., 2003. Modelling air quality in street canyons: a review. *Atmospheric Environment* 37, 155–182.
- Versteeg, H.K., Malalasekera, W., 1995. *An Introduction to Computational Fluid Dynamics: The Finite Volume Method*. Longman, Malaysia pp. 198–203 and 243–244.
- Yakhot, V., Orszag, S.A., 1986. Renormalization group analysis of turbulence. *Journal of Scientific Computing* 1, 3–51.
- Yakhot, V., Smith, L.M., 1992. The renormalization group, the  $\varepsilon$ -expansion and derivation of turbulence models. *Journal of Scientific Computing* 7, 35–61.
- Yakhot, V., Orszag, S.A., Thangam, S., Gatski, T.B., Speziale, C.G., 1992. Development of turbulence models for shear flows by a double expansion technique. *Physics of Fluids A* 4, 1510–1520.
- Zhang, Y.Q., Arya, S.P., Snyder, W.H., 1996. A comparison of numerical and physical modeling of stable atmospheric flow and dispersion around a cubical building. *Atmospheric Environment* 30, 1327–1345.